Molecular orbitals and $\alpha+^{18}$O molecular bands of ^{22}Ne

Masaaki Kimura
Yukawa Institute for Theoretical Physics, Kyoto University, Kyoto 606-8502, Japan
(Received 22 October 2005; revised manuscript received 19 October 2006; published 23 March 2007)

Focusing on α clustering, the structure of ^{22}Ne was studied. We predict the presence of the molecular orbital bands that have an $\alpha+^{16}$O cluster core surrounded by two neutrons occupying the molecular orbitals, together with $\alpha+^{18}$O molecular bands. The formation of the $\alpha+^{16}$O cluster core and its close relation to the configuration of two valence neutrons are discussed.

DOI: 10.1103/PhysRevC.75.034312 PACS number(s): 21.60.Gx, 27.30.+t

I. INTRODUCTION

Nuclear clustering is one of the most essential degrees of freedom of nuclear excitation, and many experimental and theoretical studies have been devoted to understanding its nature. Since the early 1990s, the study of the clustering aspects in $N \neq Z$ nuclei has been greatly developed, and various new exotic aspects have been discovered. Much of this new information on nuclear clustering in $N \neq Z$ nuclei provides not only deeper understanding of the clustering itself but also the knowledge of its coupling with other degrees of freedom such as the single-particle motion of valence neutrons. One such example is 2α clustering of Be isotopes. The cluster model studies [1–5] and the antisymmetrized molecular dynamics (AMD) studies [6–8] have shown that the ground states and many excited states of Be isotopes have the 2α core and the covalently bound neutrons around the core (molecular orbital). Depending on the valence neutron configurations and on the number of the valence neutrons, the degree of the 2α clustering changes dynamically. The AMD study [8] also predicts the existence of the ^{6}He+^{6}He molecular band in ^{12}Be in which valence neutrons are not bound covalently but to either of two α particles.

Considering the variety of the 2α cluster structure of Be isotopes, it is natural to expect the $\alpha+^{16}$O clustering of Ne isotopes. For example, W. von Oertzen [9] has proposed the possible existence of the molecular orbital structure in Ne isotopes and suggested a new assignment of the rotational bands of ^{21}Ne. Compared to ^{8}Be, which has an almost pure 2α cluster structure in its ground state, ^{20}Ne has a mixture of the cluster and the shell structure in its ground and excited states [10–12]. Consequently, when we add some neutrons to ^{20}Ne, we expect to find more dynamic formation and dissolution of the $\alpha+^{16}$O cluster structure depending on the motion of the valence neutrons.

^{22}Ne is the lightest even-even $\alpha+^{16}$O+xn system and is stable nucleus. Therefore, experimental information [13–18] is rather rich compared to that from heavier Ne isotopes. Indeed, large quadrupole deformation of the ground band is well known and some excited rotational bands were experimentally investigated and theoretically discussed [19–23]. However, the theoretical interpretation of many excited states has not been established yet. In particular, experimental and theoretical information on α clustering of this nucleus is not enough compared to ^{20}Ne. Experimentally, to my knowledge, α clustering in ^{22}Ne was investigated first by W. Scholz *et al.* [24,25] based on the α transfer reaction on ^{18}O. They reported the significant α clustering of 10 natural parity states lying between 6.24 and 8.59 MeV (3.4 and 1.0 MeV below the $\alpha+^{18}$O threshold energy). However, the theoretical interpretation of these states has not been given yet. Recently, in addition to those states, the α cluster states lying above the $\alpha+^{18}$O threshold energy are observed [26–28]. In particular, G. V. Rogachev *et al.* [26] and V. Z. Goldberg *et al.* [28] reported 1^-, 3^-, 7^-, and 9^- states that are the member states of the $\alpha+^{18}$O molecular band above the $\alpha+^{18}$O threshold energy. This $\alpha+^{18}$O molecular band is theoretically discussed by P. Descouvemont and M. Dufour [29–31] based on the $\alpha+^{18}$O(J^π) extended two-cluster model (ETCM). Thus, α clustering of ^{22}Ne has been reported at least in two energy regions, a few MeV below and above $\alpha+^{18}$O threshold energy, suggests much more complicated α clustering systematics than those of the ^{20}Ne and Be isotopes.

In this article, we discuss the structure of ^{22}Ne, focusing mainly on the $\alpha+^{16}$O clustering of the core nucleus. The theoretical framework of the deformed-basis AMD (DAMD) [12] plus generator coordinate method (GCM) is combined with the $\alpha+^{18}$O cluster wave function to investigate the systematics of the α clustering of ^{22}Ne. Because the DAMD assumes no cluster structure and describes the shell, the cluster, and their mixed structure, it serves the purpose of the present study. We predict the existence of the molecular orbital bands that are possibly assigned to the α cluster states below $\alpha+^{18}$O threshold energy observed in Ref. [25]. Above the $\alpha+^{18}$O threshold energy, the existence of the $\alpha+^{18}$O molecular bands that correspond to the observed bands [26,28] are also shown.

The contents of this article are as follows. In the next section, we briefly present the framework of DAMD and propose a new constraint on the variational calculation that makes it possible to investigate various motion of the valence neutrons. In Sec. III, we present the results and discuss the structure of ^{22}Ne. Especially, we discuss the detail of α clustering and predict two different kinds of α clustering in this nucleus, the molecular orbital bands and the $\alpha+^{18}$O molecular bands. In the final section, we summarize the present study.

II. THEORETICAL FRAMEWORK

In this section, the framework of the DAMD is given and the calculational procedure applied in this study is explained.

A. Wave function and Hamiltonian

In the DAMD, the intrinsic wave function of the system with mass A is given by a Slater determinant of single-particle wave packets;

$$\Phi_{\rm int} \equiv \mathcal{A}\{\varphi_1, \varphi_2, \ldots, \varphi_A\}, \tag{1}$$

$$\varphi_i(\mathbf{r}) \equiv \phi_i(\mathbf{r})\chi_i\xi_i, \tag{2}$$

where φ_i is the ith single-particle wave packet consisting of the spatial ϕ_i, spin χ_i, and isospin ξ_i parts. The triaxially deformed Gaussian centered at $\mathbf{Z}_i$ is employed as the spatial part of the single-particle wave packet:

$$\phi_i(\mathbf{r}) \equiv \exp\left[-\sum_{\sigma=x,y,z}\nu_\sigma\left(r_\sigma - \frac{\mathrm{Z}_{i\sigma}}{\sqrt{\nu_\sigma}}\right)^2\right],$$

$$\chi_i \equiv \alpha_i\chi_\uparrow + \beta_i\chi_\downarrow, \quad |\alpha_i|^2 + |\beta_i|^2 = 1, \tag{3}$$

$$\xi_i = \text{proton} \quad \text{or} \quad \text{neutron}.$$

Here, the complex number vector parameter $\mathbf{Z}_i$ takes independent value for each nucleon. The width parameters ν_x, ν_y, and ν_z are real number parameters and take independent values for each direction but are common to all nucleons. Spin part χ_i is parametrized by α_i and β_i and isospin part ξ_i is fixed to proton or neutron. $\mathbf{Z}_i$, ν_x, ν_y, ν_z, α_i, and β_i are the variational parameters. As the variational wave function, we employ the parity projected wave function,

$$\Phi^\pm \equiv \hat{P}^\pm\Phi_{\rm int} = \frac{(1 \pm \hat{P}_x)}{2}\Phi_{\rm int}, \tag{4}$$

where $\hat{P}_x$ is the parity operator.

By using the deformed Gaussians as the single-particle wave packet, we can describe the deformed shell structure, the cluster structure, and their mixed structure within the same framework. It becomes clear when we consider two limits of the wave function included in the DAMD model space, the deformed shell limit, and the cluster limit, which are schematically illustrated in Fig. 1. In the deformed shell limit, all $\mathbf{Z}_i$ are gathered around the center of the nucleus and the single-particle wave packets are deformed. In the limit of $\mathbf{Z}_i \to 0$ the wave function becomes the eigenstate of the deformed harmonic oscillator whose oscillator lengths are identical to the width parameters of the single-particle wave packet (ν_x, ν_y, and ν_z). In the cluster limit, $\mathbf{Z}_i$ are spatially separated into several parts describing the cluster structure. The single-particle wave packets become spherical when the cluster subunits are spherical nuclei. Whether the system has the cluster structure, the shell structure or their mixed structure is determined by the variational calculation explained in the next subsection.

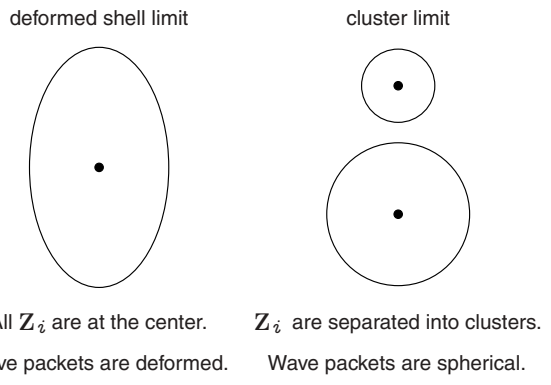

FIG. 1. Schematic figure showing two limits of the DAMD wave function. Black points indicate the centroids of the single-particle wave packets, $\mathbf{Z}_i$.

Hamiltonian used in this study is given as

$$\hat{H} = \hat{T} + \hat{V}_n + \hat{V}_c - \hat{T}_g, \tag{5}$$

where $\hat{T}$ and $\hat{T}_g$ are the kinetic energy and the energy of the center-of-mass motion, respectively. The Gogny D1S force [32] was employed as an effective nuclear force $\hat{V}_n$. The Coulomb force $\hat{V}_c$ is approximated by the sum of seven Gaussians.

B. Energy variation under the constraints

In the present work, two kinds of the constraints on the variational wave function are applied simultaneously. The first is the constraint on deformation of the system, which in the following is called the β constraint. The matter quadrupole deformation β is restricted to a certain given value β_0. It is achieved by adding a parabolic potential,

$$V_\beta = v_\beta(\beta - \beta_0)^2, \tag{6}$$

to the total energy. Here v_β is the large positive number and β denotes the matter quadrupole deformation of the variational wave function $\Phi^\pm$. The definition and the evaluation of β are given in Ref. [7].

Another one is the constraint on the number of the deformed harmonic oscillator quanta, which in the following is called the N constraint. The number operators are defined separately for proton and neutron as,

$$\hat{N}^\xi \equiv \sum_i\sum_{\sigma=x,y,z}\left(\frac{p_{\sigma i}^2}{4\hbar\nu_\sigma} + \nu_\sigma r_{\sigma i}^2\right) - \frac{3}{2}, \tag{7}$$

$$\xi = \text{proton or neutron}, \tag{8}$$

where summation over i runs all protons or all neutrons. We note that the oscillation numbers of deformed harmonic oscillator in Eq. (7) are defined by the width parameter of the single particle wave packet [Eq. (3)] as $\omega_\sigma = 2\hbar\nu_\sigma/m$. We impose some different constraints on the expectation values $N^\xi \equiv \langle\Phi^\pm|\hat{N}^\xi|\Phi^\pm\rangle/\langle\Phi^\pm|\Phi^\pm\rangle$. For example, when there is no core excitation,

$$N^{\rm val} \equiv N^n - N^p \tag{9}$$

will provide the quantum number of valence neutrons. By adding the potential,

$$V_N = v_N(N^{\rm val} - N_0)^2\,\theta(N^{\rm val} - N_0),$$

$$\theta(x) = \begin{cases} 0, & x < 0 \\ 1 & x \geqslant 0 \end{cases}, \quad v_N > 0, \tag{10}$$

to the energy of the system, $N^{\rm val}$ is restricted to less than N_0. Details of the applied N constraints are explained in

the next section. Here we make an additional comment on the N constraint. It is easily confirmed that the value of N^ξ is independent of the frequencies ω_σ and the width parameters ν_σ. It depends strongly on $\mathbf{Z}_i$ and increases as $|\mathbf{Z}_i|$ becomes large in general. Therefore N^ξ is quite sensitive to the formation of the cluster structure, because $\mathbf{Z}_i$ are distantly separated when the system has the cluster structure as shown in Fig. 1. Of course, N^ξ is also sensitive to the single particle configuration.

The variational parameters $\mathbf{Z}_i, \nu_x, \nu_y, \nu_z, \alpha_i$, and β_i are optimized under the β and N constraints so that the energy of the system plus constraint potentials,

$$E^\pm = \frac{\langle\Phi^\pm|\hat{H}|\Phi^\pm\rangle}{\langle\Phi^\pm|\Phi^\pm\rangle} + V_\beta + V_N, \tag{11}$$

is minimized. The variation is made by the frictional cooling method, which is a kind of the imaginary time development method. The time development equation for the complex parameters $\mathbf{Z}_i, \alpha_i$, and β_i is given as

$$\frac{dX_i}{dt} = \frac{\mu}{\hbar}\frac{\partial E^\pm}{\partial X_i^*}, \quad (i = 1, 2, \ldots, A), \tag{12}$$

and that for the real number parameters ν_x, ν_y, and ν_z is given as

$$\frac{d\nu_\sigma}{dt} = \frac{\mu'}{\hbar}\frac{\partial E^\pm}{\partial \nu_\sigma}, \quad (\sigma = x, y, z). \tag{13}$$

Here X_i represents $\mathbf{Z}_i, \alpha_i$, or β_i. μ and μ' are the arbitrary negative real numbers. By this method, we obtain the optimized wave function $\Phi^\pm_{\rm int}(\{\mathrm{C}\})$ under a certain combination of β- and N-constraint parameters $\{\mathrm{C}\}$. It is confirmed that at the end of the variational calculation, V_β and V_N are less than 10 keV.

C. Analysis of the single-particle orbitals

To understand the single-particle configuration, we calculate the single-particle orbitals of the optimized wave function $\Phi^\pm_{\rm int}(\{\mathrm{C}\})$. When the wave function $\Phi^\pm_{\rm int}(\{\mathrm{C}\}) = \hat{\mathrm{P}}^\pm\mathcal{A}\{\varphi_1, \varphi_2, ...\varphi_\mathrm{A}\}$ is given, we transform the single-particle wave packet φ_i to the orthonormalized basis $\widetilde{\varphi}_\alpha$,

$$\widetilde{\varphi}_\alpha \equiv \frac{1}{\sqrt{\lambda_\alpha}}\sum_{i=1}^{A} c_{i\alpha}\varphi_i. \tag{14}$$

Here, λ_α and $c_{i\alpha}$ are the eigenvalues and eigenvectors of the overlap matrix $B_{ij} \equiv \langle\phi_i|\phi_j\rangle$,

$$\sum_{j=1}^{A} B_{ij}c_{j\alpha} = \lambda_\alpha c_{i\alpha}. \tag{15}$$

Using this basis, the Hartree-Fock single-particle Hamiltonian,

$$h_{\alpha\beta} \equiv \langle\widetilde{\varphi}_\alpha|\hat{t}|\widetilde{\varphi}_b\rangle + \sum_{\gamma=1}^{A}\langle\widetilde{\varphi}_\alpha\widetilde{\varphi}_\gamma|\hat{v}_n + \hat{v}_c|\widetilde{\varphi}_\beta\widetilde{\varphi}_\gamma - \widetilde{\varphi}_\gamma\widetilde{\varphi}_\beta\rangle,$$
$$+ \frac{1}{2}\sum_{\gamma,\delta=1}^{A}\langle\widetilde{\varphi}_\gamma\widetilde{\varphi}_\delta|\widetilde{\varphi}^*_\alpha\widetilde{\varphi}_\beta\frac{\partial\hat{v}_n}{\partial\rho}|\widetilde{\varphi}_\gamma\widetilde{\varphi}_\delta - \widetilde{\varphi}_\delta\widetilde{\varphi}_\gamma\rangle, \tag{16}$$

is calculated. The eigenvalues and eigenvectors of the Hartree-Fock single-particle Hamiltonian give the single-particle energies ϵ_s and the single-particle orbitals $\widetilde{\phi}_s$,

$$\sum_{\beta=1}^{A} h_{\alpha\beta}f_{\beta s} = \epsilon_s f_{\alpha s}, \tag{17}$$

$$\widetilde{\phi}_s \equiv \sum_{\alpha=1}^{A} f_{\alpha s}\widetilde{\varphi}_\alpha. \tag{18}$$

The amount of the positive-parity component in the single-particle orbitals,

$$p^+_\alpha \equiv |\langle\widetilde{\phi}_\alpha|\hat{P}^+|\widetilde{\phi}_\alpha\rangle|^2 \tag{19}$$

is used to discuss their property.

D. Angular-momentum projection and generator coordinate method

From the optimized wave function, we project out the eigenstate of the total angular momentum J,

$$\Phi^{J\pm}_{MK}(\{\mathrm{C}\}) = \hat{P}^J_{MK}\Phi^\pm(\{\mathrm{C}\}). \tag{20}$$

Here $\hat{P}^J_{MK}$ is the total angular-momentum projector. The integrals over three Euler angles are evaluated by the numerical integration.

Finally, the wave functions $\Phi^{J\pm}_{MK}(\{\mathrm{C}\})$ which have the same parity and angular momentum but have different K and constraint parameters $\{\mathrm{C}\}$ are superposed (GCM). Then the wave function of the system is written as

$$\Phi^{J\pm}_n = c_n\Phi^{J\pm}_{MK}(\{\mathrm{C}\}) + c'_n\Phi^{J\pm}_{MK'}(\{\mathrm{C}'\}) + \ldots, \tag{21}$$

where the quantum numbers except the total angular momentum and the parity are represented by n. The coefficients $c_n, c'_n, \ldots$ are determined by the Hill-Wheeler equation,

$$\delta\left(\left\langle\Phi^{J\pm}_n\middle|\hat{H}\middle|\Phi^{J\pm}_n\right\rangle - \epsilon_n\left\langle\Phi^{J\pm}_n\middle|\Phi^{J\pm}_n\right\rangle\right) = 0. \tag{22}$$

In this work, we have also performed an extended calculation in which we employ $\alpha+^{18}\mathrm{O}_{\rm g.s.}$ Brink-type cluster wave function [33],

$$\Psi^{J\pm}_{MK}(R) = \hat{P}^{J\pm}_{MK}\mathcal{A}\left\{\phi_\alpha\left(-\frac{18}{22}R\right), \phi_{^{18}\mathrm{O}_{\rm g.s.}}\left(\frac{4}{22}R\right)\right\}, \tag{23}$$

as the basis wave function of the GCM together with the DAMD wave function. The internal wave function of the ground state of ^{18}O, $\phi_{^{18}\mathrm{O}_{\rm g.s.}}$, is calculated by DAMD and is projected to $J^\pi = 0^+$. The intercluster distance R is taken from 2 to 12 fm with an interval of 1 fm. In the following, we refer to the GCM calculation with DAMD wave functions as DAMD-GCM and that with DAMD and $\alpha+^{18}\mathrm{O}_{\rm g.s.}$ cluster wave functions as hybrid GCM.

III. RESULTS

A. Energy surfaces obtained without N constraint

We first discuss the energy surface obtained with the β constraint but without the N constraint. Figure 2(a) shows the

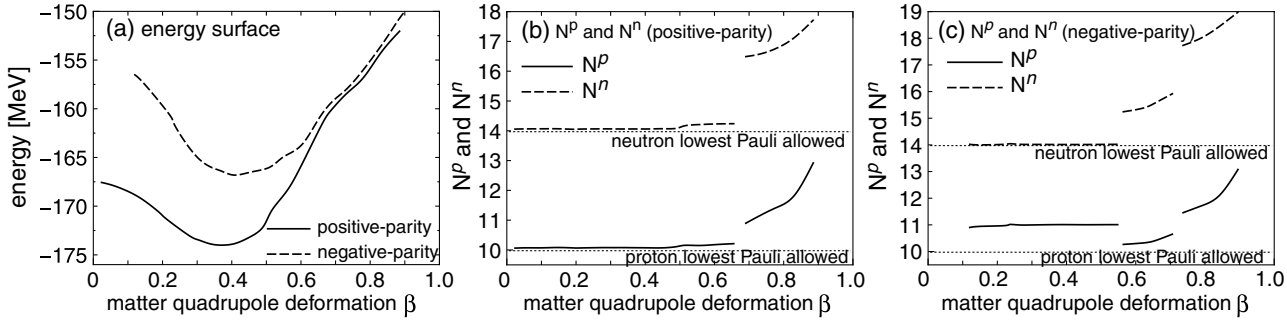

FIG. 2. (a): The energy surfaces of the positive- (solid line) and negative-parity (dashed line) states obtained without the N constraint. (b) and (c): N^p and N^n calculated from the wave functions on the energy surface of the positive-parity (b) and negative-parity (c) states.

obtained energy surfaces of the positive- and negative-parity states. At a glance, each surface has a simple structure that has a minimum energy state. However, when we see the behavior of N^p and N^n, two (three) different single particle configurations appear on the energy surface of the positive- (negative-) parity state. Figures 2(b) and 2(c) show N^p and N^n calculated from the wave functions on the energy surfaces of the positive- and negative-parity states, respectively. In the case of the positive-parity state [Fig. 2(b)], N^p and N^n have almost constant values $N^p = 10$ and $N^n = 14$ from $\beta = 0$ to 0.65. Both values are the lowest Pauli-allowed values, and hence the wave function has the $0\hbar\,\omega$ configuration. In this region, the gap between N^n and N^p that roughly corresponds to the quantum number of two valence neutrons is almost constant, $N^n - N^p \sim 4$. This means that two valence neutrons are in the sd orbitals. At $\beta = 0.65$, the structure change takes place. N^p and N^n increase discontinuously at $\beta = 0.65$ and continuously increase as deformation becomes larger. The behavior of N^p is due to the formation of the α+^{16}O cluster core and its growth as the function of β. The discontinuous increase of N^n at $\beta = 0.65$ is due to the formation of the α+^{16}O cluster core and the excitation of two valence neutrons. The gap between N^n and N^p is about 6 and shows the $2\hbar\,\omega$ excitation of two valence neutrons. The continuous increase of N^n is due to the growth of the α+^{16}O clustering. The formation of the α+^{16}O cluster core in this state will be clearly shown in the next subsection.

In the case of the negative-parity state [Fig. 2(c)], N^p and N^n have almost constant values $N^p = 11$ and $N^n = 14$ up to $\beta = 0.55$. They show the $1\hbar\,\omega$ excitation of proton, whereas neutron has the $0\hbar\,\omega$ configuration. In the region of $0.55 < \beta < 0.7$, N^p is smaller than 11, which shows the de-excitation of the proton. The gap between N^n and N^p is about 5 and shows the $1\hbar\,\omega$ excitation of a valence neutron. In the strongly deformed region $\beta > 0.7$, both N^p and N^n increase. It is due to the formation of the α+^{16}O cluster core and the excitation of two valence neutrons. The gap between N^n and N^p is about 7 and shows the $3\hbar\,\omega$ excitation of two valence neutrons.

Thus, the behavior of N^p and N^n shows that the $0\hbar\,\omega$ and the neutron $2\hbar\,\omega$ configurations appear in the positive-parity state and that the proton $1\hbar\,\omega$, the neutron $1\hbar\,\omega$ and $3\hbar\,\omega$ configurations appear in the negative-parity state.

B. Energy surfaces obtained with the N constraint and structure of wave function

We separated five different configurations discussed above by applying the N constraint. In Table I, the applied N constraints determined by referring to the results of Fig. 2 are summarized. Constraints (I) and (II) are applied to the positive-parity state. Constraint (I) keeps approximately two valence neutrons within the $0\hbar\,\omega$ configuration, whereas (II) forces the excitation of two valence neutrons. Constraints (III), (IV), and (V) are applied to the negative-parity state. Constraint (III) forces the excitation of proton, but keeps two valence neutrons within the $0\hbar\,\omega$ configuration. Constraints (IV) approximately restricts the excitation of two valence neutrons to more than $1\hbar\,\omega$ but less than $2\hbar\,\omega$, whereas (V) allows it to be more than $2\hbar\,\omega$.

The energy surfaces obtained by these five constraints are shown in Fig. 3 labeled with (I) to (V), which correspond to the applied constraints listed in Table I. All of the energy surfaces have one energy minimum state and they are referred to as

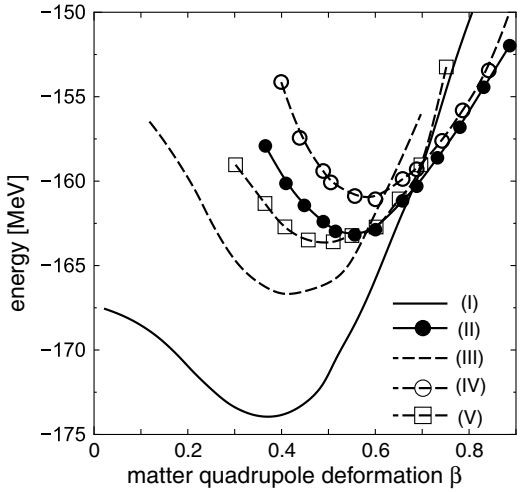

FIG. 3. The energy surfaces as the functions of the matter quadrupole deformation parameter β obtained by the N constraints (I) to (V) (see text and Table I). (I) and (II) are the positive-parity states and (III), (IV), and (V) are the negative-parity states. The energy before the angular-momentum projection is shown.

TABLE I. The five different sets of the constraints on N^p and N^n applied in this study.

Constraint	Parity	Constraint
(I)	Positive	$N^n - N^p < 4.5$
(II)	Positive	$N^n - N^p > 5.0$
(III)	Negative	$N^p > 10.5$ and $N^n - N^p < 4.5$
(IV)	Negative	$4.5 < N^n - N^p < 5.5$
(V)	Negative	$N^n - N^p > 6.0$

states (I) to (V) in the following. To understand the structure of the states (I) to (V), we investigated the single-particle configurations and the density distributions. The properties of the single-particle orbitals of the states (I) to (V) are listed in Table II. The density distributions of the core and the valence neutron orbitals are shown in Fig. 4. Here, the valence neutron orbitals are defined as the orbitals of the most weakly bound two neutrons and the core is defined as all of the remaining nucleons. It is noted that two valence neutrons occupy the orbitals that have the same density distribution except for the case of state (III).

In the case of the positive-parity state, state (I) has the $0\hbar\omega$ configuration. From the parity of the single-particle orbitals [Table II(a)], we can see that the proton and neutron orbitals No. 1 and Nos. 2 to 4 are the $0s$ and $0p$ orbitals, respectively. The proton and neutron orbital No. 5 and the neutron orbital No. 6 are the $1s0d$ orbitals. The density distribution of this state [Fig. 4(a)] shows the parity symmetric deformation of the core and the valence neutron orbitals. It also shows the absence of α clustering in this state. On the contrary, the core of state (II) has the prominent $\alpha+^{16}$O cluster structure and the parity asymmetric deformation, as shown in the density distribution [Fig.4(b)]. Due to this parity asymmetry, the parity of the single-particle orbitals [Table II(b)] is strongly mixed and it is difficult to see the correspondence to the usual spherical orbitals. Nevertheless, the density distribution of the valence neutron orbital [Fig. 4(b)] shows $1p0f$ orbital nature (it has three nodes along z axis).

TABLE II. The properties of the single-particle orbitals of states (I) to (V). The columns denoted by "No.," "occ.," "ϵ" and "p^+" show the number assigned to each single-particle orbital for the presentation, the occupation number, the single-particle energy in MeV, and the amount of the positive-parity component in percentages, respectively.

(a) State (I)

Proton				Neutron			
No.	occ.	ϵ (MeV)	p^+(%)	No.	occ.	ϵ (MeV)	p^+(%)
1	2	−41.1	100	1	2	−42.7	100
2	2	−27.8	5	2	2	−28.0	2
3	2	−21.6	6	3	2	−22.4	4
4	2	−16.0	7	4	2	−17.2	5
5	2	−12.6	100	5	2	−13.5	100
				6	2	−8.9	94

(b) State (II)

Proton				Neutron			
No.	occ.	ϵ (MeV)	p^+(%)	No.	occ.	ϵ (MeV)	p^+(%)
1	2	−38.7	93	1	2	−39.5	92
2	2	−26.1	22	2	2	−25.9	22
3	2	−18.7	20	3	2	−20.5	21
4	2	−16.5	94	4	2	−16.1	90
5	2	−13.3	29	5	2	−14.5	43
				6	2	−5.6	36

(c) State (III)

Proton				Neutron			
No.	occ.	ϵ (MeV)	p^+(%)	No.	occ.	ϵ (MeV)	p^+(%)
1	2	−41.7	100	1	2	−42.0	100
2	2	−28.6	9	2	2	−29.1	8
3	2	−21.5	10	3	2	−21.5	10
4	1	−15.9	12	4	2	−15.5	11
5	2	−13.5	90	5	2	−14.5	91
6	1	−9.7	91	6	2	−8.6	90

(d) State (IV)

Proton				Neutron			
No.	occ.	ϵ (MeV)	p^+(%)	No.	occ.	ϵ (MeV)	p^+(%)
1	2	−39.1	95	1	2	−40.5	96
2	2	−27.3	8	2	2	−27.4	10
3	2	−19.4	15	3	2	−20.8	13
4	2	−15.6	91	4	2	−15.9	70
5	2	−13.7	35	5	2	−14.5	40
				6	1	−7.9	90
				7	1	−3.4	21

(e) State (V)

Proton				Neutron			
No.	occ.	ϵ (MeV)	p^+(%)	No.	occ.	ϵ (MeV)	p^+(%)
1	2	−38.1	91	1	2	−39.1	92
2	2	−25.2	45	2	2	−23.7	44
3	2	−18.5	38	3	2	−20.2	38
4	2	−16.0	81	4	2	−16.5	83
5	2	−12.8	47	5	2	−14.1	52
				6	2	−6.5	49

In the case of the negative-parity state, state (III) shows proton excitation from the $0p$ to the $0d1s$ orbital, whereas the neutron has the $0\hbar\omega$ configuration. The occupation number and the parity of the proton single-particle orbitals [Table II(c)] show that a proton is excited from orbital No. 4 ($0p$) to orbital No. 6 ($0d1s$). Due to this proton excitation, this state does not show α clustering [Fig. 4(c)]. The core of state (IV) has the moderate $\alpha+^{16}$O cluster structure [Fig. 4(d) and 4(e)]. One of two valence neutrons occupies the excited orbital [Table II(d), No. 7, and Fig. 4(e)] which has pf orbital nature and the other occupies the $0d1s$ orbital [Table II, No. 6, and Fig. 4(d)]. The core of the state (V) has the most prominent $\alpha+^{16}$O cluster structure [Fig. 4(f)]. Again, because of the strong parity mixing, the assignment of each orbital to the spherical one is rather ambiguous. Two valence neutrons occupy the excited orbital that has the pf-orbital nature [Table II(e), No. 6, and Fig. 4(f)].

To summarize this subsection, we note the following points. The configuration of valence neutrons is controlled by applying the N constraint. This method revealed that α clustering of the core strongly depends on the configuration of two valence neutrons. Namely, the core has the $\alpha+^{16}$O cluster structure [states (II), (IV), and (V)], when one or two neutrons are excited into the orbital that has the pf-orbital nature [Figs. 4(b), 4(e), and 4(f)]. It is also interesting that the states (II) and (V) have a similar structure. They have the $\alpha+^{16}$O cluster core and two valence neutrons occupying the orbitals that have the pf-orbital nature. Indeed, in the Sec. III D, we will discuss that these two states can be considered the parity doublet partner.

TABLE III. The in-band $E2$ transition probabilities of the ground, $K^\pi = 2^+, 2^-$, 0_2^+, and 0_1^- bands in Weisskopf units. Numbers in parentheses are the experimental data taken from Refs. [16,34].

g.b.→g.b.			$K^\pi = 2^+ \to K^\pi = 2^+$		
J_i	J_f	$B(E2)$ (W.u.)	J_i	J_f	$B(E2)$ (W.u.)
2_1^+	0_1^+	14.9 (13.6±1.6)	3_1^+	2_2^+	15.5
4_1^+	2_1^+	20.5 ($20.1^{+4.3}_{-3.0}$)	4_2^+	2_2^+	5.4
6_1^+	4_1^+	15.8 ($12.8^{+3.1}_{-2.1}$)	4_2^+	3_1^+	8.4
8_1^+	6_1^+	10.8 (⩾0.02)	5_1^+	3_1^+	7.4
			5_1^+	4_2^+	11.4
$K^\pi = 2^- \to K^\pi = 2^-$			$K^\pi = 0_2^+ \to K^\pi = 0_2^+$		
J_i	J_f	$B(E2)$ (W.u.)	J_i	J_f	$B(E2)$ (W.u.)
3_1^-	2_1^-	6.5	2_3^+	0_2^+	29.0
4_1^-	2_1^-	2.1	4_3^+	2_3^+	32.1
4_1^-	3_1^-	4.5	6_2^+	4_3^+	30.9
5_1^-	3_1^-	4.1	8_2^+	6_2^+	24.4
5_1^-	4_1^-	5.1			
$K^\pi = 0_1^- \to K^\pi = 0_1^-$			$K^\pi = 1^- \to K^\pi = 1^-$		
J_i	J_f	$B(E2)$ (W.u.)	J_i	J_f	$B(E2)$ (W.u.)
3_3^-	1_2^-	41.4	2_2^-	1_1^-	11.4
5_3^-	3_3^-	47.1	3_2^-	2_2^-	12.9
7_1^-	5_3^-	46.8	3_2^-	1_1^-	13.4
9_1^-	7_1^-	43.9	4_2^-	3_2^-	16.8
			4_2^-	2_2^-	12.1

C. Level scheme and $E2$ transition probabilities

The wave functions on the energy surfaces are superposed after the angular-momentum projection and the Hamiltonian is diagonalized (DAMD-GCM). The obtained level scheme of ^{22}Ne is presented in Fig. 5 together with its experimental counterpart. The in-band $E2$ transition probabilities are also listed in Table III.

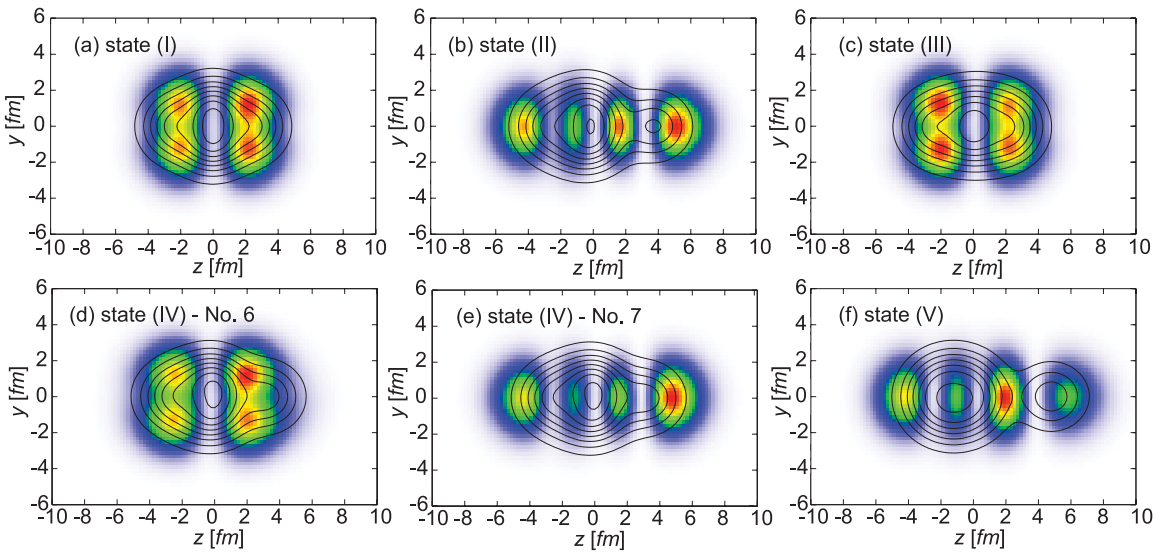

FIG. 4. (Color online) The density distributions of the core and the valence neutrons of the states (I) to (V). Contour lines show the density distribution of the core. Color plots show the density distribution of the valence neutron orbital. The density is integrated over the x axis.

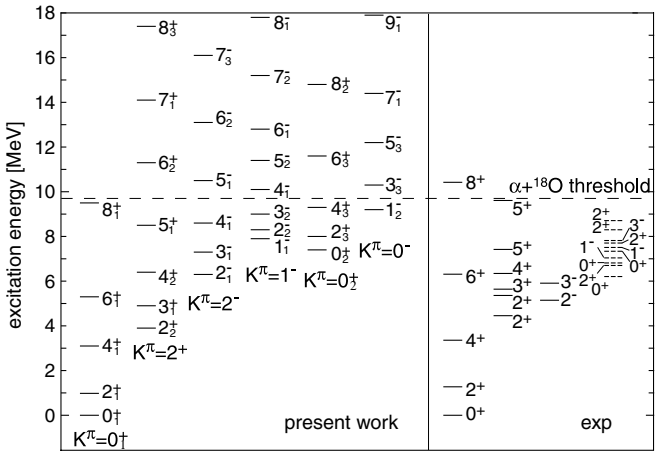

FIG. 5. Low-lying level scheme of ^{22}Ne obtained by the DAMD-GCM calculation. At the right-hand side, the experimental candidates of the present results are plotted. Dashed lines show the states that has large α reduced widths observed by the α transfer reaction [25].

The calculated ground-band ($K^\pi = 0^+_1$) spectrum shows the good agreement with the experiment, though the excitation energies of 6^+_1 and 8^+_1 states are slightly underestimated by about 1 MeV. In the present calculation, higher spin state than 8^+ is not obtained. The dominant component of the ground band is state (I) and it is not strongly mixed with the states on other energy surfaces. The in-band $E2$ transition probabilities (Table III) are also in good agreement with the experiment without using any effective charge.

TABLE IV. The calculated α reduced widths of the ground state, $K^\pi = 0^+_2, 0^-_1$, and 1^- band member states. E_x shows the excitation energy in MeV. The α reduced width is given in the unit of the Wigner limit $\theta^2_\alpha = \gamma^2_\alpha/\gamma^2_W$. The calculated and observed [25] ratios of the α reduced width to that of the ground state are also shown.

	Present work				Exp.		
J^π	Band	E_x	θ^2_α(%)	Ratio	J^π	E_x	Ratio
0^+_1	$K^\pi = 0^+_1$	0	1.7×10^{-4}	1.0	0^+_1	0	1.0
0^+_2	$K^\pi = 0^+_2$	7.2	7.4×10^{-3}	43.5	0^+	6.24	19.2
					0^+	6.90	10.8
2^+_3	$K^\pi = 0^+_2$	8.0	5.3×10^{-3}	31.2	2^+	6.82	4.6
					2^+	7.63	14.6
					2^+	8.59	76.9
4^+_3	$K^\pi = 0^+_2$	9.6	3.1×10^{-3}	18.2			
6^+_2	$K^\pi = 0^+_2$	11.9	1.8×10^{-3}	10.6			
8^+_2	$K^\pi = 0^+_2$	15.1	7.8×10^{-4}	5.2			
1^-_2	$K^\pi = 0^-_1$	9.4	1.1×10^{-2}	69.3	1^-	7.06	9.2
1^-_1	$K^\pi = 1^-_1$	7.9	1.4×10^{-3}	8.2	1^-	7.49	11.5
3^-_3	$K^\pi = 0^-_1$	10.3	8.6×10^{-3}	50.6	3^-	7.73	18.5
3^-_2	$K^\pi = 1^-_1$	9.0	1.0×10^{-3}	5.9			
5^-_3	$K^\pi = 0^-_1$	12.4	3.4×10^{-3}	20.7			
5^-_2	$K^\pi = 1^-_1$	11.5	2.9×10^{-4}	1.7			
7^-_1	$K^\pi = 0^-_1$	14.6	9.5×10^{-4}	5.6			
7^-_2	$K^\pi = 1^-_1$	15.4	1.2×10^{-4}	0.7			
9^-_1	$K^\pi = 0^-_1$	18.5	6.6×10^{-3}	3.9			

The intrinsic wave functions on the energy surface (I) also generates the $K^\pi = 2^+$ band together with the ground band. Experimentally, this band is not well established. In Ref. [30], authors assigned the 3^+ state at 5.6 MeV and the 4^+ state at 6.3 MeV as the member states of this band based on the ETCM calculation. There are two experimental candidates for the 2^+ state (4.46 and 5.36 MeV) and the 5^+ state (7.42 and 9.61 MeV). In Ref. [30], the 2^+ state at the 4.46 MeV and the 5^+ state at 7.42 MeV are suggested as the band member states. From the present results, we cannot conclude which states are the member states of this band. For example, the 2^+ state at 4.46 MeV shows a better fit with our result in the excitation energy, but in this choice, the 2^+, 3^+, and 4^+ states deviate from the rotational spectrum, whereas our result shows the rotational character. Experimental information such as $E2$ transition probability will fix the assignment of this band.

The obtained lowest negative-parity band is the $K^\pi = 2^-$ band which is built on the 2^-_1 state at 6.4 MeV. We have assigned the observed 2^- state at 5.1 MeV and 3^- state at 5.9 MeV as the member states of this band. The higher spin states of this band have not been observed, though there are some candidates whose spin-parity have not been surely fixed yet. This band purely consists of the wave functions on the energy surface (III) that have the $1\hbar\omega$ proton excitation. Experimentally, there is no information about the single-particle configuration of this band. However, it is rather natural that the lowest negative-parity band has a proton hole in the $0p$ orbital, because it is known that the lowest negative-parity band of ^{20}Ne, $K^\pi = 2^-$, also has a hole in the $0p$-orbital.

Other three rotational bands $K^\pi = 1^-$, 0^+_2, and 0^-_1 have the α-cluster structure. The $K^\pi = 1^-$ band mainly consists of the wave functions on the energy surface (IV) in which one of two neutron is excited to the pf orbital. The natural parity states of this band have small mixing with the wave function on the energy surface (III). The $K^\pi = 0^+_2$ band almost purely consists of the wave functions on the surface (II) in which two valence neutrons are excited into the pf orbital. The $K^\pi = 0^-_1$ band consists of the wave functions on the surface (V) and has the most prominent α clustering among obtained bands. The α clustering brings about the strong in-band $E2$ transition probabilities in the $K^\pi = 1^-$, 0^+_2, and 0^-_1 bands.

D. Molecular orbital bands

In this subsection, we focus on three rotational bands, $K^\pi = 1^-$, 0^+_2, and 0^-_1, that have the α+^{16}O cluster core and one or two excited valence neutrons. To understand structure of them, we investigate the neutron single-particle orbitals of state (V), which is the dominant component of the $K^\pi = 0^-_1$ band in detail. Figure 6 shows all of the neutron single-particle orbitals of state (V). Two neutrons occupy each orbital. Figure 6(a) shows the most deeply bound neutron orbital that, of course, shows the $0s$ orbital nature. However, we see that the centroid of the density distribution is not at the center of the system but at the center of the ^{16}O cluster. This means that orbital No. 1 is nothing but the $0s$ orbital inside the ^{16}O cluster. In the same

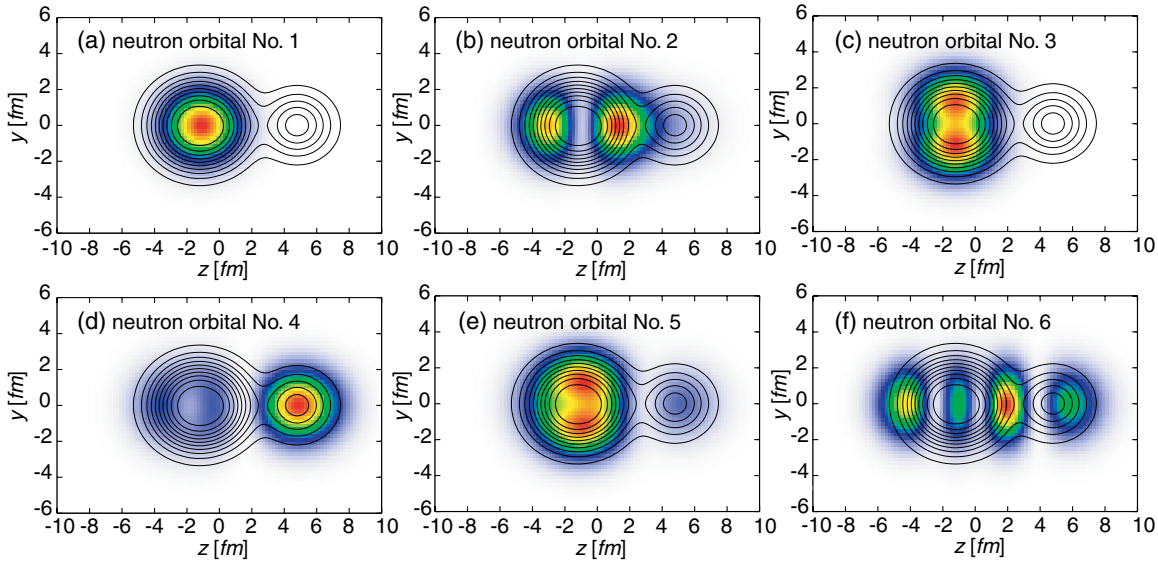

FIG. 6. (Color online) The density distributions of the core and the neutron single-particle orbitals Nos. 1 to 6 of state (V). Contour lines show the density distribution of the core and are common to all figures. Color plots show the density distribution of the neutron orbital Nos. 1 (a) to 6 (f).

way, neutron orbital Nos. 2, 3, and 5 [Figs. 6(b), 6(c), and 6(e)] are understood as the $0p$ orbitals of the ^{16}O cluster. Orbital No. 4 [Fig. 6(d)] is at the center of the α cluster, and hence it is the $0s$ orbital inside the α cluster. Thus, the neutron orbitals Nos. 1 to 5 approximately correspond to the single-particle orbitals inside the α or ^{16}O clusters. This characteristic structure of the neutron orbital Nos. 1 to 5 explains why it was difficult to understand them from their parity [Table II(e)]. Here, we note that there is small mixing between the single-particle orbitals inside of the α and ^{16}O clusters [typically between Figs. 6(d) and 6(e)]. It indicates the weak interaction between clusters and suggests that the α+^{16}O subsystem could be unbound if they did not have the valence neutrons, because of a too-weak interaction between them.

In contrast to other neutrons, two valence neutrons go around the entire system and interact with both clusters to bind the total system [Fig. 6(f)]. It should be noted that the 1^-_2 state (the band head of $K^\pi = 0^-_1$) is bound much deeper than the α+^{16}O + $2n$ threshold energy and even deeper than the α+^{18}O threshold energy, despite the weak interaction between the α and ^{16}O clusters. This valence neutron orbital is an analog of the σ molecular orbital of Be isotopes in the following sense. (1) The neutron in this orbital binds two clusters. (2) This orbital is, for the most part, composed of the orbitals around the clusters (Fig. 7). In the case of Be isotopes, the σ orbital is composed of the $0p$ orbitals around two α clusters. In the present case, it is composed of the $0p$ orbital around the α cluster and the $1s0d$ orbital around the ^{16}O cluster. This type of molecular orbital is also suggested in Ref. [9] in the case of ^{21}Ne. (3) The neutron in this orbital induces the α clustering of the core. In the case of Be isotopes, it enlarges the distance between two α. In the present case, as already discussed, it induces the formation of the α+^{16}O cluster core. When one neutron occupies this orbital [state (IV)] the core has the α+^{16}O cluster structure. When two neutrons occupy this orbital [states (II) and (V)], the α+^{16}O clustering is enhanced. Because of these similarities, we call this neutron orbital the σ orbital in the following.

The most prominent difference between the σ orbital of Be isotopes and that of ^{22}Ne is the parity asymmetry of the present one, that is induced by the parity asymmetry of the core. The parity asymmetry leads to the presence of the parity doublet bands. The state (II) that is the dominant component of the $K^\pi = 0^+_2$ band has a quite similar structure to that of state (V). It also has weakly interacting α+^{16}O cluster core surrounded by two valence neutrons in the σ orbital. Therefore, the $K^\pi = 0^+_2$ and 0^-_1 bands can be understood as the parity doublet bands. Surprisingly, the energy gap between

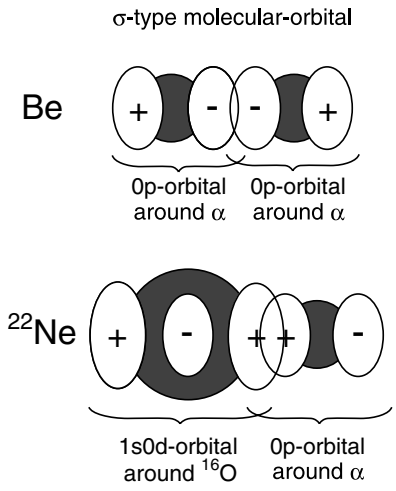

FIG. 7. The schematic figure showing the σ molecular orbitals of the Be isotopes and ^{22}Ne. Black circles show the core clusters and white circles show the σ molecular orbital.

the band head states of the $K^\pi = 0_2^+$ and 0_1^- bands is quite small (about 2 MeV). It is much smaller than that between the $K^\pi = 0_1^\pm$ bands of ^{20}Ne (5.8 MeV). The small energy gap is understood as follows. First, the parity doublet bands of ^{22}Ne lie in higher excitation energy than those of ^{20}Ne. The higher excitation energy causes more prominent clustering. Second, more importantly, two valence neutrons prohibit the α and ^{16}O clusters being close to each other due to the Pauli principle that acts between neutrons in the σ orbital and the clusters. They also prohibit the dissolution of the α+^{16}O core. Indeed, the energy surfaces (II) and (V) in Fig. 3 are steeper than surface (I) for smaller deformation. Even in the small deformed region of surfaces (II) and (V), the core still has the α+^{16}O cluster structure. It is in contrast to the ground band of ^{20}Ne in which the α+^{16}O cluster structure dissolves when the intercluster distance becomes small [12]. In other words, two valence neutrons in the σ orbital provide the potential barrier against the inversion motion, whose height is the origin of the small energy gap. This effect does not exist in the case of ^{20}Ne.

Experimentally, there is information neither about the assignment of the $K^\pi = 1^-, 0_2^+$, and 0_1^- bands, nor about the presence of the molecular orbital bands. However, it was reported by W. Scholz *et al.* [24] that several states with the significant α clustering existed between 6.24 and 8.59 MeV. In Table IV, the α-reduced widths of $K^\pi = 1^-, 0_2^+$, and 0_1^- bands and their ratios to the ground state are shown together with the observed ratios. Here, the α reduced width γ_α^2 is defined as

$$\gamma_\alpha^2 = \frac{\hbar}{2\mu a}|a\mathcal{Y}_L(a)|^2, \tag{24}$$

The reduced width amplitude $\mathcal{Y}_L(r)$ is evaluated by taking the overlap between the wave function of each state and the set of the α+^{18}O(0_1^+) Brink-type wave functions [33] as explained in Refs. [8,12]. The channel radius is taken as $a = 5$ fm. It is notable that the calculated molecular orbital bands and the observed states show similar nature. They appear a few MeV below the α+^{18}O threshold energy, and they have 10 times larger α reduced widths than the ground state. Therefore, we consider that those observed states are the promising candidates of the molecular orbital bands discussed here.

TABLE V. The calculated α reduced widths of the $K^\pi = 0_3^+$ and 0_2^- bands. E_x denotes the excitation energy in MeV. The α reduced width is given in the unit of the Wigner limit $\theta_\alpha^2 = \gamma_\alpha^2/\gamma_W^2$. The results of the ETCM calculation [31] and the experimental data [26,28] are also shown. Only the upper and lower bounds of the fragmented stetes are shown for the experimental 1^- and 3^- states [28].

Hybrid GCM			ETCM [31]			Exp. [26,28]		
J^π	E_x	θ_α^2(%)	J^π	E_x	θ_α^2(%)	J^π	E_x	θ_α^2(%)
1_3^-	14.8	8.7	1^-	12.58	13	1^-	11.88–12.82	2–12
			1^-	12.84	8			
3_4^-	15.2	9.1	3^-	12.92	13	3^-	12.70–13.57	1–13
			3^-	13.69	11			
5_4^-	16.8	9.0	5^-	13.68	23			
			5^-	14.69	100			
7_3^-	18.9	10.3	7^-	18.79	52	7^-	19.28	8
			7^-	19.56	81	7^-	19.56	5
9_2^-	22.5	11.7				9^-	20.85	51
						9^-	21.84	57

E. α + ^{18}O molecular bands

Recently, the other type of the α clustering, α+^{18}O molecular band, is studied experimentally and theoretically by some authors [26–31]. Experimentally, the $K^\pi = 0^\pm$ bands start from a few MeV above the α+^{18}O threshold energy. The member states are fragmented into several states. These observed states are shown in Fig. 8 by connected squares together with the ground band. Theoretically, these bands are investigated in Refs. [29–31]. Therefore, the relation between these α+^{18}O molecular bands and the molecular orbital bands discussed above is questioned. Especially, one may think that they could be identical.

By the DAMD-GCM calculation, we did not obtain α+^{18}O molecular bands in the observed energy region. It is because the DAMD wave functions employed as the GCM basis do not have the α+^{18}O cluster structure. To complete our calculation, we have performed the hybrid-GCM calculation by including the α+^{18}O cluster model wave functions into the GCM basis. Here we included only the elastic channel α+^{18}O$_{g.s.}$, because it was shown in Refs. [29–31] that this channel dominates the α+^{18}O molecular bands. The obtained bands are shown in Fig. 8 with connected circles. The bands that do not have the α-cluster structure are not shown for the presentation except for the ground band. The α+^{18}O$_{g.s.}$ cluster wave function

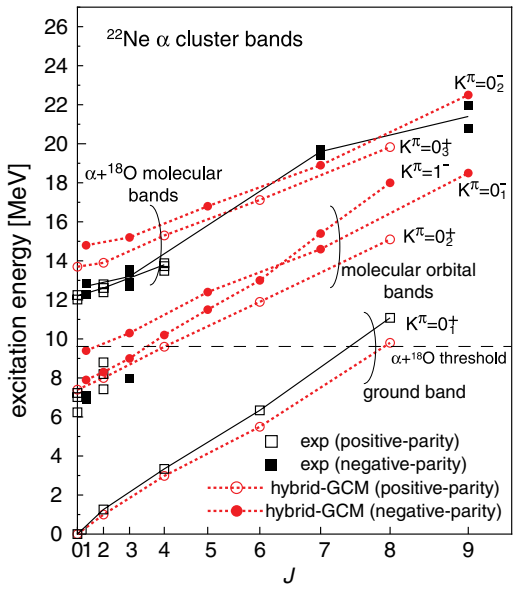

FIG. 8. (Color online) The level scheme of the ground band and the rotational bands that have the α+^{16}O cluster core. Open (filled) circles show the positive- (negative-) parity states obtained by the hybrid GCM. Open (filled) squares connected with lines show the experimental spectrum of the ground band and the α+^{18}O molecular bands [26,28]. Disconnected squares show the observed states by the α-transfer reaction [25].

is mixed mainly with the DAMD wave functions on the energy surfaces (I), (II), and (V). The hybrid GCM gives two additional rotational bands $K^\pi = 0_3^+$ and 0_2^- above the $\alpha+^{18}$O threshold energy, together with other rotational bands that are also obtained by the DAMD-GCM. The calculated excitation energy and α reduced widths of the $K^\pi = 0_3^+$ and 0_2^- bands (Table V) are comparable with the experimental data and with the ETCM calculation [31]. Therefore, the calculated $K^\pi = 0_3^+$ and 0_2^- bands correspond to the observed $\alpha+^{18}$O molecular bands. We have not obtained the fragmentation of the member states of these bands. This may be due to the lack of other channel such as $\alpha+^{18}\mathrm{O}(2_1^+)$ in the hybrid GCM. The properties of other bands, including the molecular orbital bands obtained by the hybrid GCM, are almost the same as those obtained by the DAMD-GCM. Therefore, the observed $\alpha+^{18}$O molecular bands and the molecular orbital bands predicted in this study are not identical. Indeed, their excitation energies are different and their α reduced widths are different in the order of magnitude.

The hybrid-GCM result suggests that there are two kinds of the α-cluster structure in ^{22}Ne. The first one is the molecular orbital bands that have the $\alpha+^{16}$O cluster core and two valence neutrons go around the entire system to bind the system. They start from the states below the $\alpha+^{18}$O threshold energy. The second one is the $\alpha+^{18}$O molecular bands in which two neutrons go around the ^{16}O cluster. They start from the states above the $\alpha+^{18}$O threshold energy.

IV. SUMMARY

In this work, the low-lying level scheme of ^{22}Ne has been investigated by the DAMD-GCM and the hybrid GCM. By applying the N constraint, the states with different single-particle configurations and different structures are obtained. The properties of the ground band is successfully described and the known experimental data are reproduced. The low-lying $K^\pi = 2^+$ band with $(sd)^6$ configuration and $K^\pi = 2^-$ band with $\pi(0p)^{-1}(sd)^3$ configuration are also suggested.

It is found that depending on the configurations of two valence neutrons, the $\alpha+^{16}$O cluster structure is formed and dissolved in the core nucleus ^{20}Ne. When one or two neutrons occupy the σ orbital, the $\alpha+^{16}$O cluster core develops. We predict the presence of the molecular orbital bands $K^\pi = 1^-, 0_2^+$, and 0_1^-, in which the valence neutrons in the σ orbital bind the weakly interacting α and ^{16}O clusters. These bands start form the states below the $\alpha+^{18}$O threshold energy and they can be assigned to the observed α cluster states below the $\alpha+^{18}$O threshold energy reported in Refs. [24,25]. The σ orbital of ^{22}Ne is an analog of that of Be isotopes. The most prominent charactor of the σ orbital of ^{22}Ne is its parity asymmetry. It leads to the presence of the parity doublet bands $K^\pi = 0_2^+$ and 0_1^- in which two valence neutrons occupy the σ orbital. By the hybrid GCM, the $\alpha+^{18}$O molecular bands are also obtained. They correspond to the observed $\alpha+^{18}$O molecular bands reported in Refs. [26,28].

Thus we suggest two different kinds of α cluster states in ^{22}Ne, the molecular orbital bands below the $\alpha+^{18}$O threshold energy and the $\alpha+^{18}$O molecular bands above the threshold energy.

ACKNOWLEDGMENTS

The author thanks to Prof. Y. Kanada-En'yo, Prof. N. Itagaki, and Dr. M. Ito for the fruitful discussions. He also thanks Prof. H. Horiuchi and K. Ikeda for their kind encouragement. Many of the computational calculations were carried out by the SX-5 supercomputer at the Research Center for Nuclear Physics, Osaka University (RCNP). This work was performed under the Research Project for Study of Unstable Nuclei from Nuclear Cluster Aspectsh sponsored by Institute of Physical and Chemical Research (RIKEN).

[1] M. Seya, M. Kohno, and S. Nagata, Prog. Theor. Phys. **65**, 204 (1981).
[2] W. von Oertzen, Z. Phys. A **354**, 37 (1996).
[3] W. von Oertzen, Z. Phys. A **357**, 355 (1997).
[4] N. Itagaki and S. Okabe, Phys. Rev. C **61**, 044306 (2000).
[5] P. Descouvemont, Nucl. Phys. **A699**, 463 (2002).
[6] Y. Kanada-En'yo, H. Horiuchi, and A. Ono, Phys. Rev. C **52**, 628 (1995).
[7] A. Dote, H. Horiuchi, and Y. Kanada-En'yo, Phys. Rev. C **56**, 1844 (1997).
[8] Y. Kanada-En'yo and H. Horiuchi, Phys. Rev. C **68**, 014319 (2003).
[9] W. von Oertzen, Eur. Phys. J. A **11**, 403 (2001).
[10] Y. Fujiwara, H. Horiuchi, K. Ikeda, M. Kamimura, K. Katō, Y. Suzuki, and E. Uegaki, Suppl. Prog. Theor. Phys. **68**, 29 (1980).
[11] M. Dufour, P. Descouvemont, and D. Baye, Phys. Rev. C **50**, 795 (1994).
[12] M. Kimura, Phys. Rev. C **69**, 044319 (2004).
[13] D. Powers, H. T. Bair, J. L. C. Ford, and H. B. Willard, Phys. Rev. **134**, B1234 (1964).
[14] S. Goldsky, M. Port, J. Graff, J. M. Thiron, and G. Chouraqui, J. Phys. (Paris) **29**, 271 (1968).
[15] P. Neogy, R. Middleton, and W. Scholz, Phys. Rev. C **6**, 885 (1972).
[16] H. P. Trautvetter, M. Wiescher, K.-U. Kettner, and C. Rolfs, Nucl. Phys. **A297**, 489 (1978).
[17] L. D. Oliver, W. A. Richter, J. A. Stander, and J. W. Koen, Z. Phys. A **347**, 99 (1993).
[18] Z. Q. Mao and H. T. Fortune, Phys. Rev. C **50**, 2116 (1994).
[19] J. E. Stover, Nucl. Phys. **A92**, 209 (1967).
[20] Y. Akiyama, A. Arima, and T. Sebe, Nucl. Phys. **A138**, 273 (1969).
[21] L. Satpathy, D. Goss, and M. K. Banerjee, Phys. Rev. **183**, 887 (1969).
[22] B. H. Wildenthal, J. B. McGrory, and P. W. M. Glaudemans, Phys. Rev. Lett. **26**, 96 (1971).
[23] B. M. Preedom and B. H. Wildenthal, Phys. Rev. C **6**, 1633 (1972).
[24] W. Scholz, P. Neogy, K. Bethge, and R. Middleton, Phys. Rev. Lett. **22**, 949 (1969).

[25] W. Scholz, P. Neogy, K. Bethge, and R. Middleton, Phys. Rev. C **6**, 893 (1972).
[26] G. V. Rogachev *et al*., Phys. Rev. C **64**, 051302(R) (2001).
[27] N. Curtis, D. D. Caussyn, C. Chandler, M. W. Cooper, N. R. Fletcher, R. W. Laird, and J. Pavan, Phys. Rev. C **66**, 024315 (2002).
[28] V. Z. Goldberg *et al*., Phys. Rev. C **69**, 024602 (2004).
[29] P. Descouvemont, Phys. Rev. C **38**, 2397 (1988).
[30] M. Dufour and P. Descouvemont, Nucl. Phys. **A726**, 53 (2003).
[31] M. Dufour and P. Descouvemont, Nucl. Phys. **A738**, 447 (2004).
[32] J. Dechargé and D. Gogny, Phys. Rev. C **21**, 1568 (1980).
[33] D. Brink, in *Proceedings of the International School of Physics Enrico Fermi*, Course 36, Varenna 1965, edited by C. Bloch (Academic Press, New York, 1966), p. 247.
[34] P. M. Endt, Nucl. Phys. **A633**, 1 (1998).